Pure Appl. Geophys. 173 (2016), 3065–3084

DOI 10.1007/s00024-016-1324-x

Pure and Applied Geophysics

In Situ Balloon-Borne Ice Particle Imaging in High-Latitude Cirrus

Thomas Kuhn[1] and Andrew J. Heymsfield[2]

Abstract—Cirrus clouds reflect incoming solar radiation, creating a cooling effect. At the same time, these clouds absorb the infrared radiation from the Earth, creating a greenhouse effect. The net effect, crucial for radiative transfer, depends on the cirrus microphysical properties, such as particle size distributions and particle shapes. Knowledge of these cloud properties is also needed for calibrating and validating passive and active remote sensors. Ice particles of sizes below 100 μm are inherently difficult to measure with aircraft-mounted probes due to issues with resolution, sizing, and size-dependent sampling volume. Furthermore, artefacts are produced by shattering of particles on the leading surfaces of the aircraft probes when particles several hundred microns or larger are present. Here, we report on a series of balloon-borne in situ measurements that were carried out at a high-latitude location, Kiruna in northern Sweden (68N 21E). The method used here avoids these issues experienced with the aircraft probes. Furthermore, with a balloon-borne instrument, data are collected as vertical profiles, more useful for calibrating or evaluating remote sensing measurements than data collected along horizontal traverses. Particles are collected on an oil-coated film at a sampling speed given directly by the ascending rate of the balloon, 4 m s^{-1}. The collecting film is advanced uniformly inside the instrument so that an always unused section of the film is exposed to ice particles, which are measured by imaging shortly after sampling. The high optical resolution of about 4 μm together with a pixel resolution of 1.65 μm allows particle detection at sizes of 10 μm and larger. For particles that are 20 μm (12 pixel) in size or larger, the shape can be recognized. The sampling volume, 130 cm^3 s^{-1}, is well defined and independent of particle size. With the encountered number concentrations of between 4 and 400 L^{-1}, this required about 90- to 4-s sampling times to determine particle size distributions of cloud layers. Depending on how ice particles vary through the cloud, several layers per cloud with relatively uniform properties have been analysed. Preliminary results of the balloon campaign, targeting upper tropospheric, cold cirrus clouds, are presented here. Ice particles in these clouds were predominantly very small, with a median size of measured particles of around 50 μm and about 80 % of all particles below 100 μm in size. The properties of the particle size distributions at temperatures between −36 and −67 °C have been studied, as well as particle areas, extinction coefficients, and their shapes (area ratios). Gamma and log-normal distribution functions could be fitted to all measured particle size distributions achieving very good correlation with coefficients R of up to 0.95. Each distribution features one distinct mode. With decreasing temperature, the mode diameter decreases exponentially, whereas the total number concentration increases by two orders of magnitude with decreasing temperature in the same range. The high concentrations at cold temperatures also caused larger extinction coefficients, directly determined from cross-sectional areas of single ice particles, than at warmer temperatures. The mass of particles has been estimated from area and size. Ice water content (IWC) and effective diameters are then determined from the data. IWC did vary only between 1×10^{-3} and 5×10^{-3} g m^{-3} at temperatures below −40 °C and did not show a clear temperature trend. These measurements are part of an ongoing study.

Key words: Cirrus, small ice particles, in situ measurements, volume extinction coefficient, IWC, balloon-borne measurement.

1. Introduction

The sizes and shapes of tropospheric ice particles can strongly influence the Earth's climate because of their effect on incoming solar and outgoing long-wave radiation. Cirrus clouds occur at high altitudes, where they particularly influence net radiative forcing: they absorb long-wave radiation from below and, as they are cold and high, emit little infrared radiation. This greenhouse effect warms the Earth–atmosphere system. In addition, these thin ice clouds have a cooling effect from reflecting incoming solar short wave radiation. The net effect is crucial for the atmosphere, particularly at high latitudes, but will depend highly on the cloud's properties and ice particle microphysical properties such as size and shape. The large variety of ice particles in cirrus clouds makes the prediction of their effect on atmospheric radiative transfer a particular challenge.

The size distributions themselves (as opposed to average or effective sizes) are required for accurate

[1] Department of Computer Science, Electrical and Space Engineering, Luleå University of Technology, Kiruna, Sweden. E-mail: thomas.kuhn@ltu.se
[2] National Center for Atmospheric Research, Boulder, CO, USA.

radiative transfer calculations (Mitchell *et al*. 2011). The shapes of the ice particles are also potentially very important for radiative transfer. Optical properties such as light scattering by these particles are not only affected by their size distributions, but also strongly by their shapes (e.g. Baum *et al*. 2011). Thus, the ability to measure the shape and size of ice particles and their distributions under the same conditions is particularly valuable. This can be achieved directly from in situ imaging of the ice particles. A review of some of the recent aircraft- and balloon-borne in situ measurement campaigns can be found for example in Heymsfield *et al*. (2004, 2008), Schmitt and Heymsfield (2009) and Heymsfield *et al*. (2013). However, the frequently used 2D-C probe (Knollenberg 1981), an optical array probe, only records the shadow of particles passing in front of a one-dimensional photo-detector array. With a relatively poor resolution (one pixel ≈ 25 μm), it has a limited capability to measure small ice particles that characterize cold ice clouds and it is prone to sizing errors mostly affecting small particles (Korolev *et al*. 1991; Strapp *et al*. 2001). Diffraction effects for out-of-focus images cause sizing errors that increase with decreasing particle size; in addition, particles may be missed or registered as several small ones instead of one larger particle (Korolev *et al*. 1998). Due to high aircraft speed, the particles may shatter at the inlet causing fragments to appear like smaller particles, which has to be corrected for (Field *et al*. 2006) or avoided by specially modified probe tips (Korolev *et al*. 2011). The cloud particle imager, CPI (Lawson *et al*. 2001) has a much better pixel resolution (2.3 μm) and, especially for in-focus images, more structural information on ice particles can be obtained. However, ice particles below about 100 μm in size are mostly classified as "irregular" and "spheroids" (e.g. Baker and Lawson 2006a) partly due to difficulties in retrieving more detailed information for these smaller particles whose shape remains uncertain (Stoelinga *et al*. 2007). Also, the probe's sample volume, required to determine particle concentration, is not well defined (Baumgardner and Korolev 1997). Other instruments used on aircraft are the NCAR video ice particle sampler probe VIPS (McFarquhar and Heymsfield 1996) that uses video imaging of ice particles collected by impaction on an oil-coated film strip or the Cloudscope (Meyers and Hallett 2001) that images ice crystals impacting on a sapphire window. The latter can also observe airborne particles such as nuclei down to a size of 1 μm and provides the possibility to study evaporation or growth characteristics of particles.

The problems encountered with particle shattering on aircraft probes are avoided with balloon-borne measurements with an ascent rate of around 4 m s^{-1}. Ice cloud replicators have long been used both on aircraft (for example, MacCready and Todd 1964; Spyers-Duran and Braham 1967) and on balloons (for example, Magono and Tazawa 1966). The NCAR balloon-borne ice crystal replicator (Miloshevich and Heymsfield 1997) samples ice particles and preserves their shapes on a film strip coated with Formvar (polyvinyl formal, a liquid plastic when applied). The particles can then be imaged in the laboratory using conventional microscopy and stored for decades for later scientific investigations. The pixel resolution is therefore good (1–3 μm) and structural details can be retrieved from images, since all particles are in focus. Hence, all sizing uncertainties of the optical array probes are avoided. In addition, the replicator has an order of magnitude larger sample volume for small particles below (100 μm in size) than the CPI and 2D-C probes. Also, measurements on tethered balloon systems have been performed, as for example by Lawson *et al*. (2011) who raised a modified version of the aircraft instrument CPI through mixed-phase low-level clouds in polar regions on an up to 2 km long tether. These, as also the other balloon-borne measurements, have the advantage of acquiring directly vertical profiles, or quasi-vertical profiles (when the balloon is advecting together with clouds), of microphysical properties of clouds. This is very useful when studying radiative properties or calibrating or evaluating remote sensing measurements. While such useful data have been collected with the tethered balloon system, it has issues with the collection efficiency, and hence with quantitative measurements, due to dependence on particle size and wind speed (Lawson *et al*. 2011; Sikand *et al*. 2013).

Here, we present a balloon-borne in situ measurement, carried out in a several-year campaign that was recently started in northern Sweden. One of the

primary goals with this measurement campaign is to provide more data on the properties of high-latitude cirrus. While there have been some studies in the Arctic (e.g. Heymsfield *et al*. 2013; Schiller *et al*. 2008; Korolev *et al*. 1999; Krämer *et al*. 2016), data in this important region are still limited. A focus of our measurements is also to reliably measure ice particles well below 100 μm in size, which will allow studying cloud microphysical processes. This is facilitated further by the quasi-vertical profiles that are sampled with the balloon-borne instrument ascending vertically through the cloud layers, as it is moving horizontally at the same speed of the cloud. The campaign is ongoing and more valuable data will be collected in the near future adding to the existing data set that is presented here. The focus of this paper is to show the method and the usefulness of the growing data set. Section 2 describes the campaign details and the instrument. Section 3 presents and discusses the first results showing the capabilities of these balloon-borne measurements.

2. Balloon Campaign

2.1. Campaign Details

We are conducting a series of balloon-borne experiments launched into the upper tropospheric, cold ice clouds in the north of Sweden. In these experiments, we sample individual ice particles and measure their properties. The balloon launches are carried out at Esrange Space Center (67.9°N 21.1°E) located about 30 km east of Kiruna. To lift the payload, a 500 m^3 plastic balloon is used. The ascent speed is approximately 4 m s^{-1}. Measurements are performed during ascent, which usually carries the balloon eastwards, and ice clouds are sampled about 60 km away from Esrange. The ascent is terminated at an altitude of 14 km by the E-TAG system from SSC (Esrange Space Center, Sweden). The E-TAG transmits its GPS coordinates to a ground station at Esrange Space Center and is used for tracking the trajectory in real time and to find the payload during recovery. The recovery of the payload is performed by helicopter immediately after the descent on a parachute. Attached to each payload is a Vaisala radiosonde (RS92) to measure the atmospheric temperature and humidity and a video camera to confirm the presence of clouds by qualitatively assessing visibility.

The first launch was carried out in 2012 and since then each year about two launches have been done. The campaign is ongoing with more launches planned until 2019. All launches have been carried out during the winter–spring period with completely snow-covered ground. This allowed for relatively soft landings of the payload. Hence, so far no major damage occurred, so that the instrument could easily be re-used. Therefore, also future experiments are being planned during this colder season.

The meteorological conditions during all balloon launches were characterized by the frontal systems that caused large-scale cooling and ice cloud formation due to slow updrafts. Winds at ice cloud level (at and above 500 hPa) were from north-west to west. The conditions were as follows: occlusions on 2012-04-04 and 2013-12-18 with winds from north-west to west, respectively; cold front with wind from north-west on 2012-02-20; and warm front with wind from west on 2014-03-20.

2.2. Balloon-Borne Instrument

The instrument is shown in Fig. 1 and is similar to the balloon-borne replicator (Miloshevich and Heymsfield 1997) using a film strip that is uniformly advanced inside the instrument, with a short section of the film exposed to ice cloud particles underneath the inlet. Here, the film is coated with silicone oil to ensure impacting particles will stay on the film. Shortly after collection, particles are imaged inside the instrument. The imaging system consists of a microscope objective, a tube lens, and a CCD camera with 1280 × 960 pixel. Pixel resolution is 1.65 μm, and optical resolution is approximately 4 μm. The optics is focused slightly above the film strip so that all particles will be in focus. With this system, particles of 10 μm size and larger can be measured, and from about 20 μm (12 pixel across) the shape can be recognized. The collection efficiency of the NCAR replicator was modelled and confirmed in the wind tunnel to be 50 % at about 30 μm (Miloshevich and Heymsfield 1997). Our instrument uses a narrower

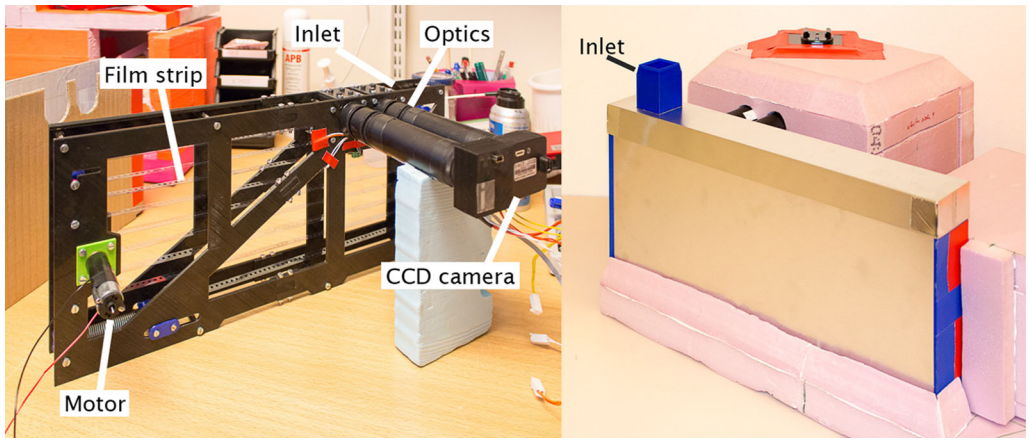

Figure 1
Pictures showing the instrument. *Left panel* instrument without enclosure showing the film strip, motor, optics, and CCD. The *horizontally arranged optics* includes a mirror so that particles on the film are viewed and imaged as seen from above. *Right panel* instrument inside enclosure. The styrofoam-insulated *box* at the back contains the CCD camera, computer and electronics, and battery. The motor with its controller and own battery are in separate foam insulation, seen on the *right* of this panel. The particle *inlet* opening is on the *left*

film strip of only 8 mm width compared to 35 mm for the replicator. Therefore in our case, the particle Stokes numbers are larger and consequently sampling of small particles is more efficient. Using the impaction studies by RANZ and WONG (1952) and GOLOVIN and PUTNAM (1962), who predict correctly the sampling efficiencies for the replicator, we found the collection efficiency in our instrument to be 50 % at about 12 μm and 80 % at around 25 μm.

Images are acquired at a frame rate of approximately 1 s^{-1}, and the film is advanced at about 1.1 mm s^{-1}. This, together with the field of view of 1280 × 1.65 μm = 2.1 mm, allows to take a complete image of a continuous stripe on the film, including some overlap. The film speed is determined more accurately from this sequence of images by the film's perforation, which can be seen on the images. After removing the perforation from the 960 pixel high images, a usable image slice that is 660 pixel high remains for analysis, corresponding to 1.1 mm on the film.

The inlet opening is 31 mm long. At a distance of another 31 mm from the inlet, the film is imaged. From these distances and the film speed, the times when particles were collected are determined for each image. Then, since the altitude of the balloon instrument and the atmospheric conditions are known at any time from radiosonde data, altitude, pressure, temperature, and relative humidity are determined for each image as well.

The sample volume is given by the 31 mm inlet opening, the 660 pixel usable image height, and the balloon's ascent rate. Particles larger than about 10 μm are collected (see collection efficiency above) and imaged if they fall inside this area, as the balloon instrument is ascending. Thus, the ascending speed of approximately 4 m s^{-1} yields a sample volume rate of 130 cm^3 s^{-1}, independent of particle size. The sample volume is only dependent on variations in the ascent speed, which are known and can therefore easily be accounted for. A known sample volume for all particles down to a size of 10 μm is a clear advantage over other instruments that are used on aircraft to measure cirrus ice particles. The forward scattering spectrometer probe (FSSP), which can measure the smallest ice particles, has a sampling volume of only around 5 cm^3 s^{-1} (at aircraft speed of 100 m s^{-1}) that is optically defined and needs to be calibrated (BAUMGARDNER *et al.* 1992). A similar instrument, the cloud aerosol spectrometer (CAS), has a somewhat larger sample volume with about 12 cm^3 s^{-1} (BAUMGARDNER *et al.* 2001). These spectrometer probes cannot measure the shape directly. Optical array probes suffer from a size-dependent

sampling volume, because the depth of the field depends on the particle size (Korolev *et al*. 1991). Additionally, out-of focus particles can cause optical breakup of particles on the image into smaller fragments that are counted erroneously as smaller particles (Field *et al*. 2006; Korolev *et al*. 1998). These problems introduce ulterior uncertainties in data analysis that already has to account for issues with particle shattering due to high sampling speeds (Field *et al*. 2006). With a pixel resolution of 25 μm, they cannot reliably measure particles of 100 μm and smaller. The 2D-S probe, a recent stereo-viewing probe combining two optical array probes in one, has a 10 μm pixel resolution. Detecting particles that small, however, is problematic given the image quality of the shadow graphs and the above-mentioned issues of optical array probes that even after more sophisticated data analysis leave uncertainties (Lawson 2011). Also, new anti-shattering tips can mitigate the problem of particle breakup; however they do not eliminate it entirely (Jackson *et al*. 2014).

2.3. Image Analysis

The first step of the particle image analysis is the detection of particles on the images, which is done manually due to irregularities on the background that make automated analysis difficult. The border of the particles on the images is traced by hand, aided by photo editing software, and the obtained contours are filled in black and saved on a white background. These resulting black-and-white images allow for automation of the next step, which is done by user-written Matlab programs that detect these black-and-white particles and trace their border line, hence providing sizes and cross-sectional areas A. The method has been described in detail by Kuhn *et al*. (2012). As the size parameter, we use the maximum dimension D, defined as the diameter of the smallest circle that completely encloses the cross-sectional area of the particle. The area ratios for individual particles are computed from the area and maximum dimension. Area ratio, Ar, is defined as the ratio of the cross-sectional area of the particle to the area of the circle whose diameter equals the maximum dimension.

From these single particle properties, the Matlab code also computes number concentrations, particle size distributions (PSD), volume extinction coefficients, and optical depths. Mass estimates of single particles are calculated from mass–dimensional and mass–area relationships.

3. Results

In this section, the first results are shown and these data are analysed. While the data set collected so far is limited, the discussion of the analysis results demonstrates the capabilities of these balloon-borne measurements.

3.1. Particle Images

Typical particles from different clouds during four experiments are shown in Figs. 2, 3, 4, 5. The temperatures were −51 °C and colder apart from cloud bases that were warmer on two occasions. In general, it can be seen that particles get larger from cloud top to base. At the cloud tops with the lowest temperatures, the smallest particles and the highest concentrations were found. More details on cloud height and temperature are given in the figures' captions.

3.2. Particle Size Distributions (PSDs)

The data are divided into several cloud layers that are not equally spaced. The division is selected after visual inspection of the data, so that layers with relatively uniform particle properties are selected. In each cloud, about three layers are analysed. Particles from each layer are then considered as particle ensembles, and the PSD of each ensemble is determined and presented in this section. In addition, the total number concentration, volume extinction coefficient, and particle size range are determined for each PSD ensemble. These properties are summarized in Table 1 and presented in the following sections.

PSDs for data from 2012-04-04 and 2013-02-20 are shown in Figs. 6 and 7. The concentrations, normalized by the widths of the equally spaced size bins, are plotted on a logarithmic scale for better inter-comparison between the PSDs. Each PSD is

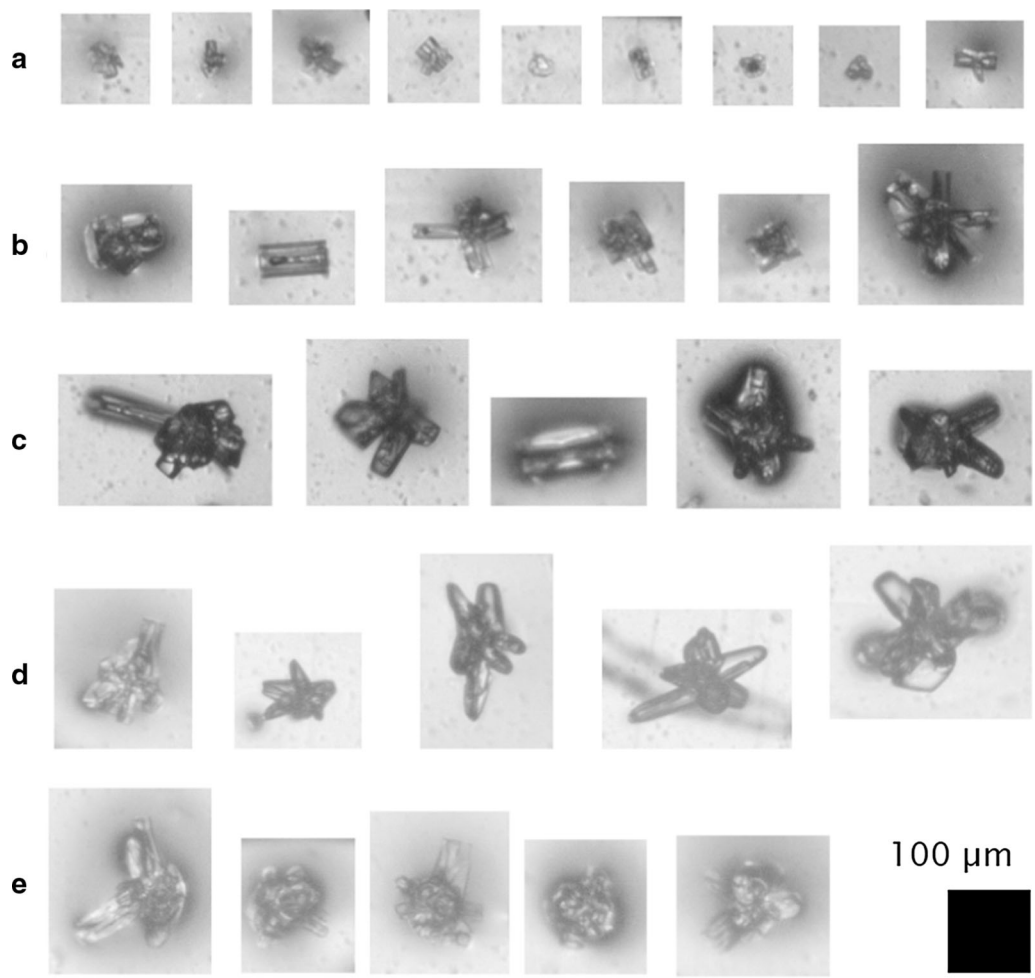

Figure 2
Typical particles from the approximately 1.7 km-thick ice cloud (**a**–**e**) measured on 2012-04-04 between 470 and 360 hPa within (**a**–**c**) a 600 m layer that was separated by about 100 m from (**d**, **e**) *bottom layer* of 1 km. *Each row* shows particles from a certain layer, starting from the cloud *top*: **a** altitude from 6940 to 7270 m, temperature around −55 °C; **b** 6860–6940 m, −53 °C; **c** 6660–6860 m, −51 °C; **d** 5680–6540 m, −46 °C; **e** 5540–5680 m, −42 °C

compared to the best fits to two commonly used distributions, the gamma distribution and the log-normal distributions, respectively, according to the following equations:

$$\text{Gamma}: N(D) = N_0 D^{\mu} \mathrm{e}^{-\lambda D}, \tag{1a}$$

$$\text{Log-normal}: N(D) = \frac{N_t}{D\sigma\sqrt{2\pi}} \exp\left(-\frac{\ln\left(\frac{D}{D_0}\right)^2}{2\sigma^2}\right), \tag{1b}$$

where in Eq. (1a) N_0 is the intercept, μ the dispersion, and λ the slope, and D the maximum dimension in units of cm (Heymsfield *et al*. 2002); σ and D_0 are the shape factor and the mode of the log-normal distribution, respectively. The total number concentration N_t is taken from the measurements. The parameters found in these fits together with the correlation coefficients R are listed in Table 2, which also shows results from fits to an area–dimensional power law (see Sect. 3.5). The best fitting gamma distribution is shown as a thin line with the same colour as the corresponding PSD, whereas the best fitting log-normal distributions are shown as thin grey lines in Figs. 6, 7. In addition, in each figure the gamma function from the parameterization by Heymsfield

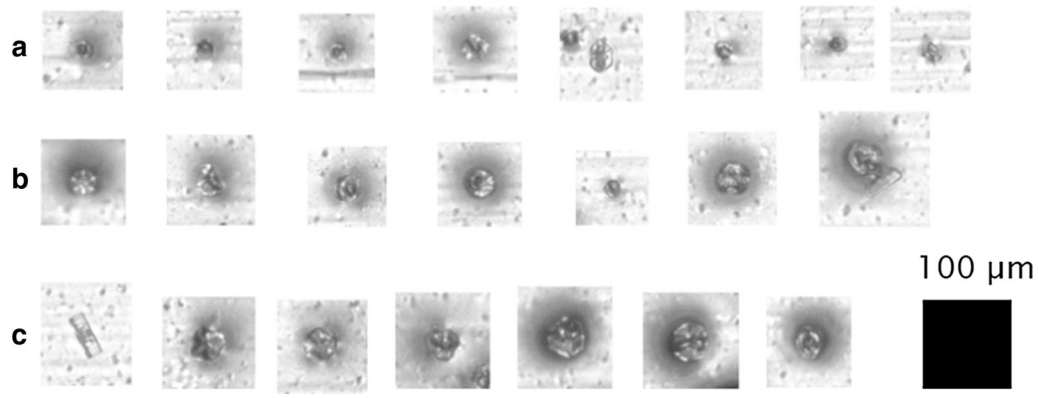

Figure 3
Typical particles from the approximately 1.1 km-thick, continuous ice cloud measured on 2013-02-20 between 300 and 280 hPa. *Each row* shows particles from a certain layer, starting from the cloud *top*: **a** altitude from 10,050 to 10,400 m, temperature around −66 °C; **b** 9600–10,000 m, −62 °C; **c** 8950–9300 m, −57 °C

Figure 4
Typical particles from the approximately 0.5 km-thick ice cloud measured on 2013-12-18 between 360 and 330 hPa. Altitude from 7550 to 8050 m, temperature around −51 °C

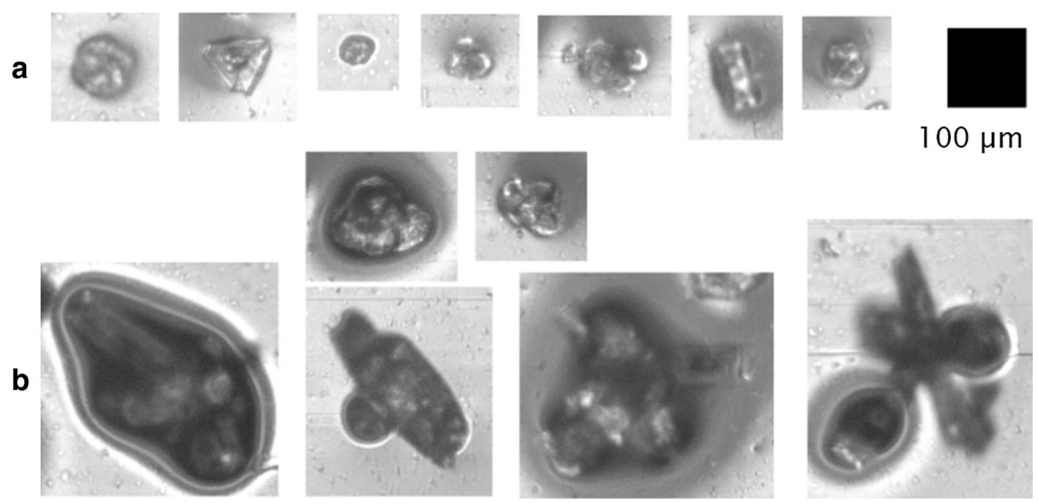

Figure 5
Typical particles from the approximately 2.3 km-thick, continuous ice cloud measured on 2014-03-20 between 440 and 310 hPa. *Each row* shows particles from a certain layer, starting from the cloud top: **a** altitude from 8250 to 8300 m, temperature around −54 °C; **b** 6000–6200 m, −36 °C

Table 1

Properties of the analysed particle ensembles

T (°C)	p (hPa)	No. of part.	N_t (m^{-3})	Extinct. (m^{-1})	IWC (g m^{-3})	d_eff (μm)	Min. D (μm)	Max. D (μm)
2012-04-04								
−54.5	369	284	1.31E+05	1.72E−04	1.97E−03	37.5	7.4	137
−53.1	383	93	3.20E+04	2.20E−04	3.72E−03	55.4	24.5	176
−51.8	392	87	1.05E+04	1.85E−04	4.03E−03	71.3	51.5	327
−45.5	440	45	4.11E+03	6.92E−05	1.50E−03	70.8	28.0	230
−42.4	466	38	7.88E+03	5.28E−05	9.02E−04	55.9	36.0	172
2013-02-20								
−66.3	243	93	3.73E+05	2.55E−04	2.11E−03	27.1	15.2	57
−62.8	261	106	2.25E+05	2.82E−04	2.87E−03	33.3	14.2	78
−57.8	287	80	8.59E+04	2.17E−04	2.62E−03	39.6	23.7	91
2013-12-18								
−52.6	335	46	1.61E+04	1.20E−04	2.18E−03	59.5	23.7	277
2014-03-20								
−57.2	299	112	4.55E+04	1.82E−04	2.76E−03	49.7	11.1	203
−54.4	313	127	5.64E+04	3.12E−04	5.27E−03	55.2	16.3	222
−36.2	433	77	1.14E+04	4.66E−04	1.32E−02	92.8	34.9	492

Temperature T and pressure p are averaged over the ensemble, and the number of analysed particles in each ensemble is stated. The size ranges are provided by the minimum and maximum particle size D (maximum dimension) encountered in the ensemble

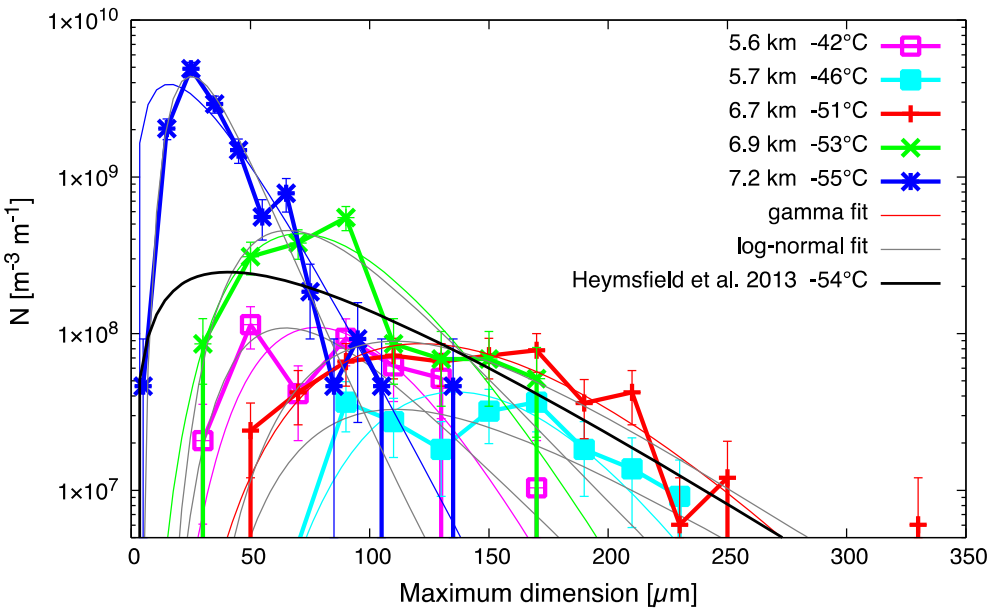

Figure 6

PSDs of different cloud layers from measurements on 2012-04-04. For each measured PSD fitted gamma and log-normal distributions are shown (*thin solid line* of the same *colour* as the corresponding PSD and *grey line*, respectively). One gamma distribution from a parameterization by HEYMSFIELD *et al.* (2013) is shown for a temperature typical for the cloud on that day (*black solid line*)

et al. (2013) for stratiform clouds is shown for a temperature typical for that cloud.

The ice cloud measured on 2012-04-04 was analysed in five layers. The bottom of the cloud (two layers) was separated by a 100 m gap from the upper part of the cloud (three layers). The corresponding five PSDs are shown in Fig. 6. The parameterization by HEYMSFIELD *et al.* (2013), shown

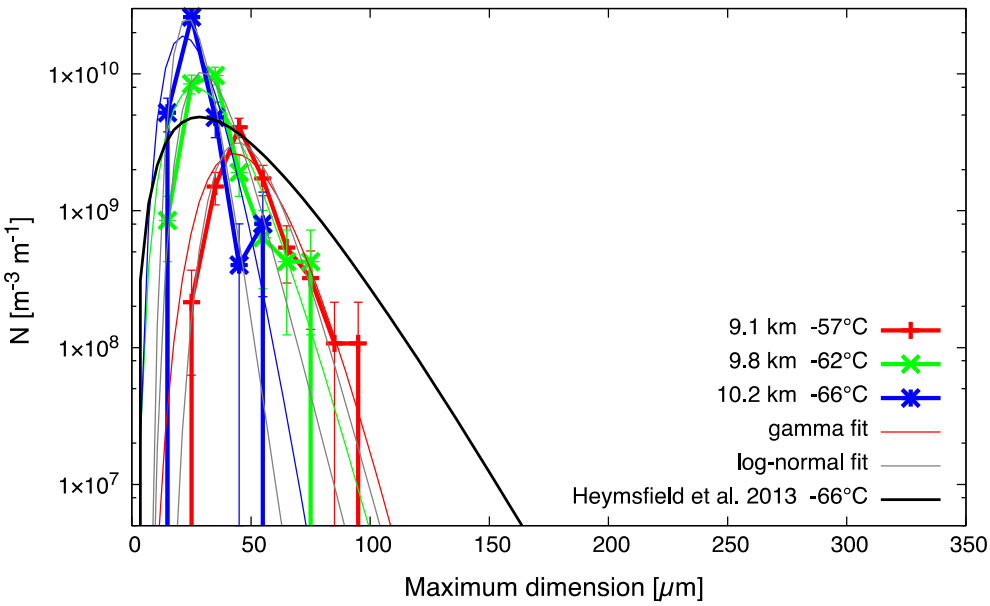

Figure 7
As for Fig. 6, but PSDs from 2013-02-20

Table 2

Fit parameters from gamma (Eq. 1a) and log-normal functions (Eq. 1b) fitted to the measured PSDs with corresponding correlation coefficients R

T (°C)	Gamma						Log normal					Area–dimensional (Eq. 5)		
	λ (cm)	N_0 (cm^{-4})	μ	R	R (area)	R (mass)	D_0 (μm)	σ	R	R (area)	R (mass)	β	α	R^2
2012-04-04														
−54.5	757	2.98E+05	1.2	0.744	0.795	0.900	30.3	4.32E−01	0.932	0.942	0.955	1.81	9.41E−13	0.962
−53.1	845	1.15E+16	5.96	0.844	0.851	0.888	76.7	3.95E−01	0.876	0.891	0.919	1.8	1.12E−12	0.962
−51.8	537	1.91E+15	6.53	0.858	0.883	0.901	129	3.92E−01	0.877	0.908	0.928	1.65	2.42E−12	0.917
−45.5	1001	8.84E+30	13.61	0.761	0.928	0.945	131.6	4.13E−01	0.677	0.902	0.929	1.66	2.08E−12	0.904
−42.4	1045	4.89E+20	8.12	0.864	0.944	0.952	76.7	4.10E−01	0.855	0.929	0.947	1.82	9.52E−13	0.935
2013-02-20														
−66.3	3261	1.19E+24	7.03	0.825	0.683	0.647	24.5	2.42E−01	0.85	0.738	0.700	1.65	1.58E−12	0.863
−62.8	1947	2.54E+17	5.15	0.819	0.791	0.855	31.8	2.85E−01	0.907	0.881	0.893	1.78	1.16E−12	0.919
−57.8	2441	7.48E+30	10.52	0.892	0.856	0.875	47	2.37E−01	0.949	0.921	0.922	1.66	1.99E−12	0.863
2013-12-18														
−52.6	258	2.80E+02	0.7	0.525	0.709	0.837	75.2	4.68E−01	0.754	0.843	0.869	1.92	6.37E−13	0.925
2014-03-20														
−57.2	472	1.58E+05	1.46	0.824	0.847	0.924	54.1	4.81E−01	0.909	0.959	0.969	1.9	7.22E−13	0.971
−54.4	449	4.39E+06	2.09	0.915	0.911	0.939	66	4.65E−01	0.829	0.922	0.939	1.82	9.58E−13	0.913
−36.2	216	9.27E+06	3.2	0.684	0.833	0.889	174.2	5.00E−01	0.711	0.866	0.907	1.88	8.10E−13	0.902

The coefficients R for area and mass distributions are also given in the table (see text in Sects. 3.5 and 3.6 for explanation). The last three columns list the parameters α and β from the area–dimensional power law given by Eq. (5) together with corresponding correlation coefficients R^2

in the figure, changes with temperature; however, changes are much smaller than the variations seen between the measured PSDs. This variation is most likely caused by micro-physical processes within the cloud. Heymsfield and Miloshevich (1995) observed the replicator profiles of cirrus clouds that had regions

of higher concentration with smaller ice particles near the cloud top, regions of growth inside the cloud, and regions of sublimation near the cloud base. They explained these trends as ice nucleation occurring at the top of an existing cloud caused by an updraft, followed by growth, and by sedimentation of larger particles, which eventually removes particles from the base of the cloud. Hence, these are likely also the processes responsible for the concentration and size trends observed in our PSDs. The parameterization does not include these processes and may be regarded as an average PSD over the whole cloud.

The cloud on 2013-02-20 was relatively cold and had very narrow PSDs with all particles smaller than 100 μm. Three layers were analysed and the corresponding PSDs are shown in Fig. 7. The best fits to gamma and log-normal distributions as well as a PSD from the parameterization by Heymsfield *et al.* (2013) is also shown.

On 2013-12-18, the cloud was very thin and possibly dissipating during the observations; it was analysed as one layer only. On 2014-03-20, the ice cloud was geometrically thick and contained few but larger particles at relatively warm temperatures, around −36 °C at the cloud base. They were analysed as one layer, and in addition two layers closer to the top with smaller particles and higher concentrations were examined. (PSDs from these 2 days are not shown; see Tables 1 and 2 for their properties.)

The best fits to the gamma distribution Eq. (1a) were determined by the moment matching method (Heymsfield *et al.* 2002). A correlation coefficient R indicates the quality of fit (see Table 2), which can also be assessed by visual comparison of the fitted function with the measured PSD in Figs. 6 and 7. It is 0.5 for the PSD on 2013-12-18 and 0.7 for the PSD at −36 °C on 2014-03-20. For all other PSDs, the fit was very good with R between 0.74 and 0.92. The best fits to the log-normal distribution Eq. (1b) have in most cases similar or somewhat better correlation coefficients that range from 0.68 to 0.94, with an average of 0.84 versus an average of 0.80 for gamma fits.

The mode (size at maximum number concentration) can also be used to compare our measured PSDs with the fitted distributions. Examining Figs. 6 and 7 reveals that they all agree reasonably well with the most prominent exception being the mode of the gamma distribution of the coldest PSD on 2012-04-04, which underestimates the measurements. The mode of the gamma distribution is located at μ/λ. For all PSDs it is compared, alongside the mode of the log-normal distribution, located at $D_0 \times \exp(-\sigma^2)$, to temperature in Fig. 8. Also the mode derived from parameterizations of μ and λ from Heymsfield *et al.* (2013) is shown, as well as exponential fits to the modes from gamma and log-normal distributions, respectively, which gave:

$$\text{Mode} = 1920\,\mu\text{m} \cdot \text{e}^{0.0693 \cdot T/^\circ\text{C}} \quad \text{(fit to modes of gamma distr.)}, \tag{2a}$$

$$\text{Mode} = 1130\,\mu\text{m} \cdot \text{e}^{0.0571 \cdot T/^\circ\text{C}} \quad \text{(fit to modes of log-normal distr.)}. \tag{2b}$$

3.3. Total Number Concentration

The total number concentrations for these particle ensembles are shown in Fig. 9 as a function of the ambient temperature (average during the period in which particles in the respective ensemble were collected). A trend of increasing concentrations with decreasing temperature can be seen both in general as well as during specific experiments, i.e. in specific clouds. This means that the concentrations are highest at the cloud tops, which have the lowest temperatures and probably where ice nucleation is taking place, as was suggested above (in Sect. 3.2). The total number concentrations in our particle ensembles vary by about two orders of magnitude in the covered temperature range and can be approximated by the relationship

$$N_\text{t} = 0.0185\ \text{L}^{-1} \cdot \text{e}^{-0.143 \cdot T/^\circ\text{C}}. \tag{3}$$

Heymsfield *et al.* (2013) reported a relationship, based on data from stratiform clouds from many field campaigns, with similar total number concentrations but a weaker dependence on temperature. Krämer *et al.* (2016) did not find a dependence of the number concentration on temperature. They partitioned their measurements based on model simulations of cirrus cloud origin in two types: in situ and liquid-origin cirrus. They describe the resulting different

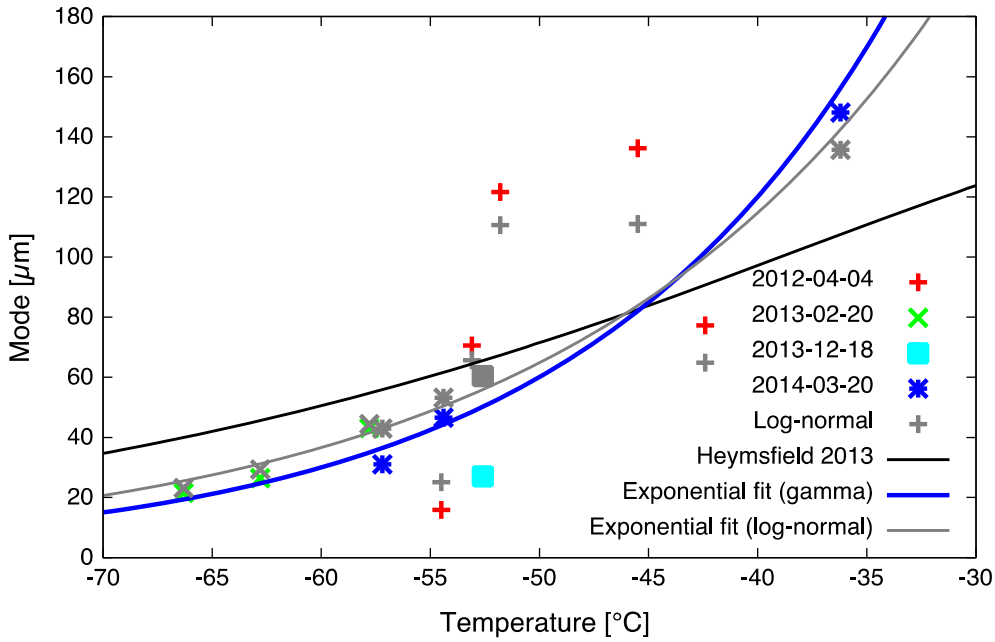

Figure 8
Modes of the gamma (shown in *colour*) and log-normal distributions fitted to the measured PSDs are shown versus average temperatures. The modes derived from the parameterizations by HEYMSFIELD *et al.* (2013) are shown as a *black line* together with fitted exponential *trend lines* given by Eqs. (2a, 2b)

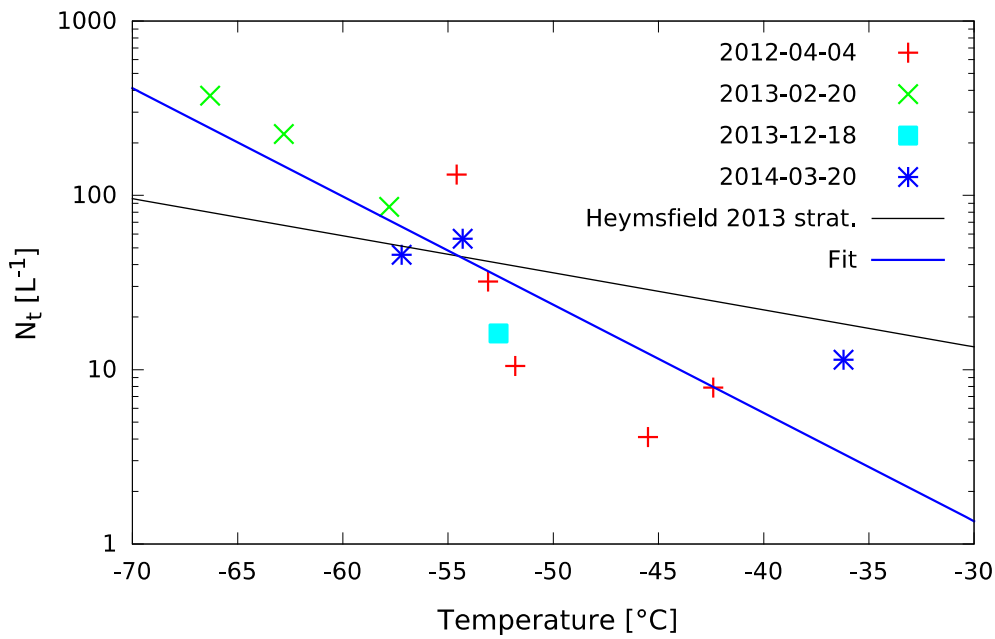

Figure 9
Total number concentration N_t versus (average) temperature. An exponential fit to the data, as well as a parameterization by HEYMSFIELD *et al.* (2013) is shown as *two lines*

microphysical properties, and in a continuation study Luebke *et al*. (2016) report number concentrations of in situ origin cirrus in a similar range as in our study with most measurements around 100 L^{-1}. Liquid-origin cirrus, on the other hand, had a median of reported number concentrations of above 100 L^{-1}. Note, however, that they used measurements from the FSSP and CAS scattering probes. Although they argue that shattering on the leading edges of the probes would be expected to be minimal due to the predominance of small particles, shattering may have contributed to the concentrations; furthermore, these probes have very small sampling volumes, and therefore these concentrations have inherent uncertainties.

3.4. Volume Extinction Coefficient and Optical Depth

Figure 10 shows the volume extinction coefficient that is twice the sum of the cross-sectional areas of all particles in the ensemble divided by the corresponding probe sampling volume. Although not as strongly as the total number concentration, also the extinction coefficient increases with decreasing temperatures, with only one noticeable exception at the warmest ensemble. This increase is caused by the increasing number concentration, which more than compensates the general trend of decreasing particle sizes and areas with decreasing temperatures. The data at temperatures colder than −40 °C can be fitted to an exponential relationship:

$$\text{Extinction coefficient} = 3.91 \times 10^{-6}\text{m}^{-1} \cdot \text{e}^{-0.0689 \cdot T/^{\circ}\text{C}}. \quad (4)$$

Optical depths can be determined from the measurements by integrating 10 s averages of extinction coefficient over altitude. For the clouds analysed it ranges from 0.01 to 0.9: on 2012-04-04 it was 0.19 (0.13 only the upper, colder cloud); on 2013-02-20 it was 0.45; on 2013-12-18 it was 0.01; and on 2014-03-20 it was approximately 0.9. Thus, the measured clouds are all optically thin and include sub-visible clouds.

3.5. Area and Area Ratio

The measured areas A of individual ice particles are plotted versus maximum dimension in Fig. 11. All data were fitted to the area–dimensional relationship

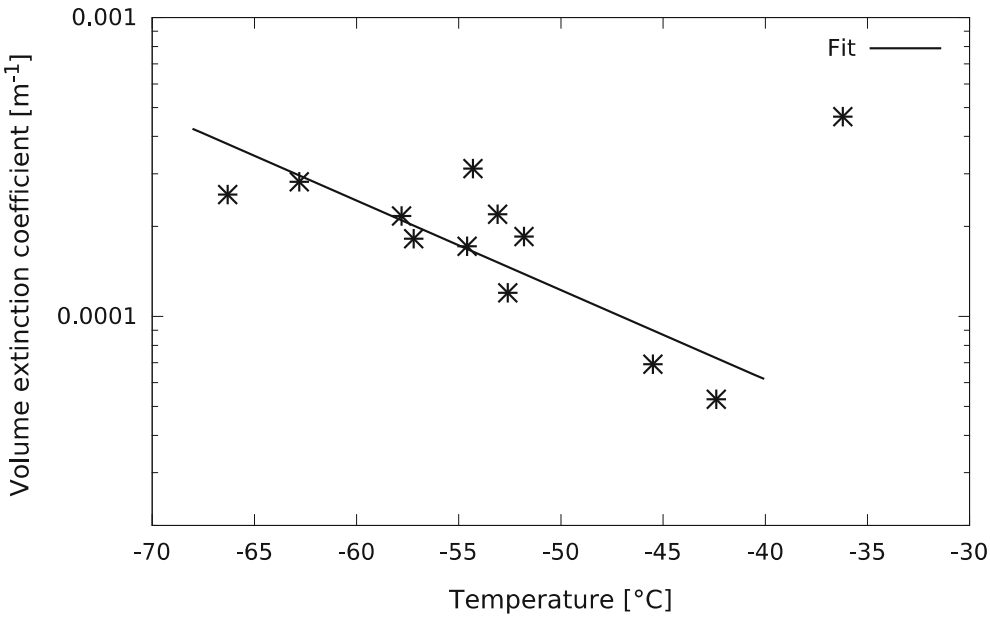

Figure 10
Volume extinction coefficient of ice particles in cloud layers versus temperature. Data below −40 °C is fitted to a *straight trend line*, Eq. (4), on the *logarithmic plot*

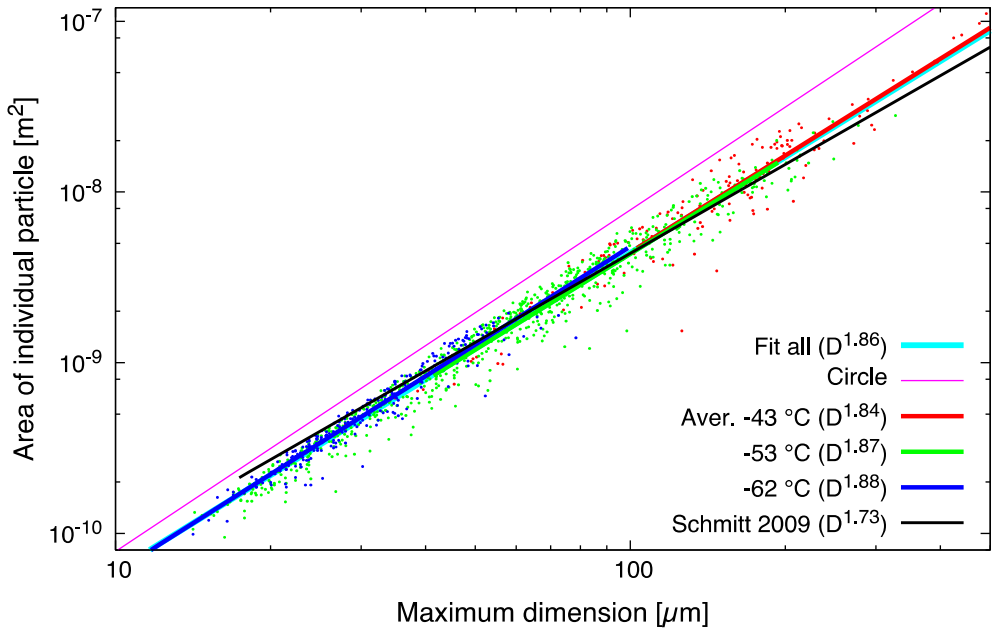

Figure 11
Measured areas A of individual ice particles are plotted versus maximum dimension D. The *data points* are shown in *different colours* in three different temperature ranges. Best fits to Eq. (5) are shown in the *same colours* for the three data groups in addition to a fit to all data. The relationship by SCHMITT and HEYMSFIELD (2009) and the areas of circles with diameter D are also shown for comparison

$$A = \alpha D^{\beta}. \quad (5)$$

The linear regression (using least square fit) between $\log A/(1\ \mathrm{m}^2)$ and $\log (D/1\ \mu\mathrm{m})$ revealed $\alpha = 8.23 \times 10^{-13}$ and $\beta = 1.86$ (with $R^2 = 0.98$). The data were also split into three continuous temperature ranges (between −35 and −50, −50 and −58, and −58 and −68 °C, respectively) having average temperatures of −43, −53, and −62 °C. In Fig. 11, the data of these three temperature ranges are plotted with three different colours. The exponents β from the fitted area–dimensional relationships are reported in the figure's legend, and the fitted relationships are also shown in the figure, in addition to the relationship for spherical particles (i.e. area of circles with diameter = maximum dimension D). The results from each temperature range alone are very similar to the best fit through all data. Since the different temperature ranges correspond to different size ranges, this means that a single power law area–dimensional relationship describes well our data from 10 to 500 μm. This can also be seen from Fig. 11: no deviation (such as a bend) from the straight line can be discerned. The relationship by SCHMITT and HEYMSFIELD (2009) does also fit well the data; however, it is less steep (has lower β) and therefore overpredicts the area for the smallest sizes and underpredicts for the largest sizes.

Figure 12 shows the area ratios Ar determined from our measurements. The same colour coding as in Fig. 11 has been used to mark the three temperature ranges. The average Ar in size bins of 20 μm width are also shown together with vertical bars that indicate the spread of the data (standard deviation).

For comparison, the area ratios reported by SCHMITT and HEYMSFIELD (2009) are shown in Fig. 12. They reported two relationships for the two size ranges above and below 200 μm, corresponding to the power law of Eq. (5) (black line) and an exponential Ar function (grey line), respectively. Of these two, the power law for maximum dimension above 200 μm agrees better with our data in the whole size range. It is also this relationship that, converted to area, is shown in Fig. 11, where it agreed better than their small particle relationship (not shown in that figure) with measured areas.

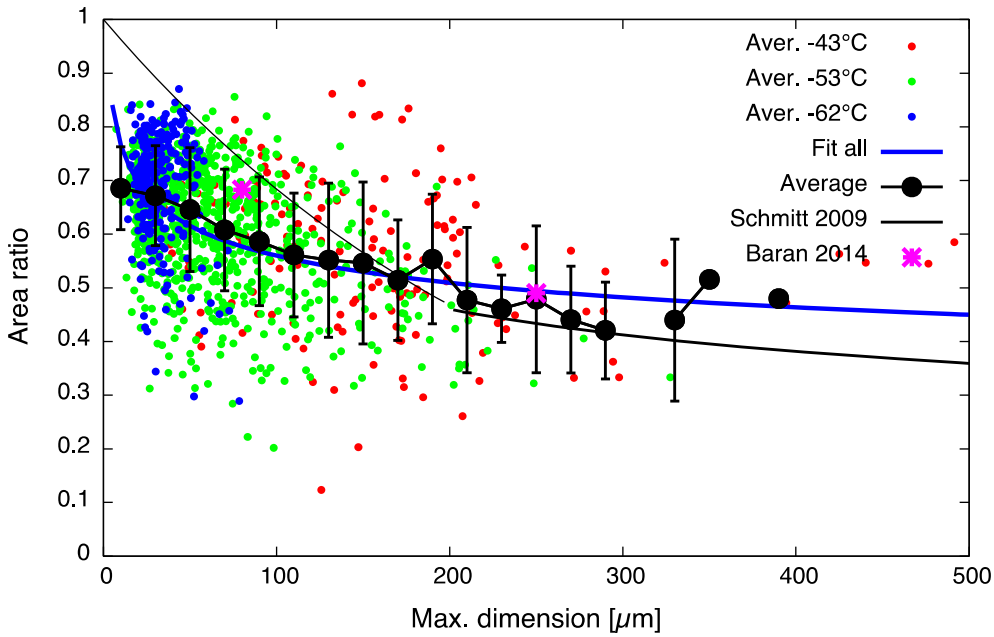

Figure 12
Area ratios Ar of individual particles (*colour coded* as in Fig. 11) and averages in size bins are shown versus maximum dimension *D*. The fit to Eq. (5) shown in Fig. 11 is also shown here, converted to Ar. The Ar parameterization by SCHMITT and HEYMSFIELD (2009) for particles larger than 200 μm is shown as a *black line*, and their parameterization for small particles as *grey line*

All our data can be approximated well by one power law relationship only, which is demonstrated by the line in Fig. 12 showing the Ar derived from the best fit to the area–dimensional relationship Eq. (5):

$$\mathrm{Ar} = 1.05 \times (D/(1\mu\mathrm{m}))^{-0.136} \qquad (6)$$

BARAN *et al.* (2015) presented recently an ensemble model of ice crystals. The area ratio of their model ice particles, which change as a function of maximum dimension, predict well the trend of increasing Ar for decreasing maximum dimension that our data reveal (see Fig. 12).

This area–dimensional power law relationship (Eq. 5) can also be used to convert the gamma and log-normal distributions fitted to our PSDs (see Sect. 3.2) to gamma and log-normal area distributions. For this, the size distributions are multiplied with area as calculated by Eq. (5). By comparing these converted area distributions to the area distributions derived directly from measurements (multiplying the concentrations in the PSDs with the measured particle area averaged over the respective size bin), it can be assessed how good the fitted number distributions describe the area or extinction of the measured ice particles. The modes of the gamma and log-normal area distributions agreed very well with the modes of the measured area distributions (correlation coefficients *R* between 0.68 and 0.94 for gamma distributions and 0.74 and 0.96 for log-normal distributions, respectively, as can be seen in Table 2).

3.6. Mass and Effective Diameter

Mass can be estimated from a mass–dimensional relationship. Then, all particles having the same size would have the same mass, even though they have quite different areas (see Fig. 11). The measured area information available for each particle would be neglected. Hence, by using area instead of maximum dimension, likely a better mass estimate can be achieved (BAKER and LAWSON 2006b). Here, we use a combination of mass–dimensional and mass–area relationships. Thus, both measured size and area are used to determine particle mass, and hence IWC. It

should be noted that this is an estimate only, since the balloon experiments used in this study did not include direct mass measurement. The area is multiplied by an effective thickness, which is calculated from the maximum dimension using a power law with an exponent below one. Heymsfield *et al.* (2013) suggested the following link between area–dimensional and mass–area relationships:

$$m \sim D^{\gamma}, \text{ with } \gamma = 1.275\beta, \tag{7}$$

where β is the exponent from Eq. (5) and m the particle mass. This relationship was based on the concept of fractal dimension of ice particles (Schmitt and Heymsfield 2010) and we consider it to be a good starting point to determine a suitable exponent to determine the effective thickness to be used in calculation of particle mass. For this, we replace $D^{1.275\beta} = D^{\beta+0.275\beta}$ with $A \times D^{0.275\beta}$, so that we can use measured area A and maximum dimension D together with $\beta = 1.86$ from the best fit to Eq. (5). The exponent is then $0.275 \times 1.86 = 0.512$. The relationship needs to be scaled so that it yields meaningful estimates of mass. We found a suitable scaling by constraining our mass estimates to be close to two literature relationships, a mass–dimensional relationships by Schmitt and Heymsfield (2009) and the mass–area relationship by Baker and Lawson (2006b). The resulting mass–area–dimensional relationship is:

$$m = \rho_{\text{ice}} A \cdot 37\mu\text{m} \cdot (D/100\,\mu\text{m})^{0.512} \quad D \geq 30\,\mu\text{m}, \tag{8a}$$

$$m = \rho_{\text{ice}} \cdot 2/3 \cdot AD \quad D < 30\,\mu\text{m}. \tag{8b}$$

In the above equations, ρ_{ice} is the bulk density of ice, 917 kg m^{-3}. At a certain size, the area–mass conversion Eq. (8a) becomes the same as for a spherical particle. With our scaling this happens at $D = 30$ µm. Therefore, below 30 µm we use this spherical particle relationship given by Eq. (8b) (Eq. 8a would otherwise predict a larger mass below 30 µm). These mass estimates are shown in Fig. 13.

Using the mass–area–dimensional relationship given by Eqs. (8a, 8b), the fitted gamma or log-normal distributions can be converted to mass distributions. The area A in Eqs. (8a, 8b) is calculated

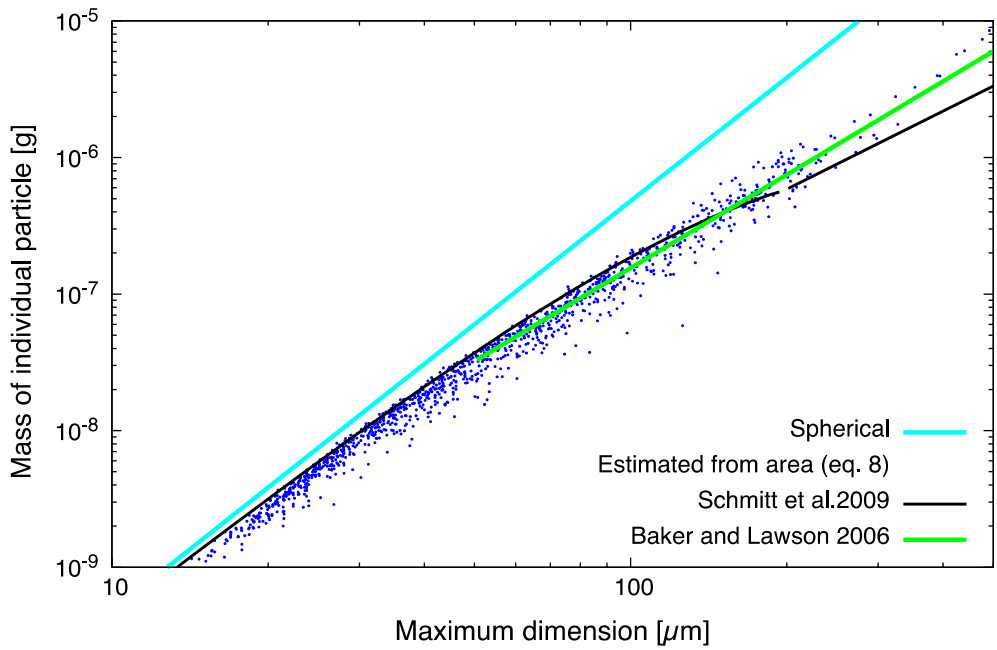

Figure 13
Mass of individual ice particles estimated from their area A and maximum dimension D plotted versus D. The mass–dimensional relationship by Schmitt and Heymsfield (2009) and the mass–area relationship by Baker and Lawson (2006b) are shown for comparison. The latter uses the area from Eq. (5) fitted to all data

for this purpose using Eq. (5). These mass distributions derived from the fitted functions can then be compared to the mass distributions derived from the measured PSDs and Eqs. (8a, 8b) with measured A (averaged from all single particles in each size bin), similarly as done earlier with area distributions (Sect. 3.5). As for area, also for mass, the distributions agree well among each other, and correlation coefficients between mass distributions derived directly from measurements and gamma or log-normal mass distributions, respectively, are very high (between 0.65 and 0.95 for gamma distributions and 0.70 and 0.97 for log-normal distributions, respectively, as can be seen in Table 2).

Figure 14 shows the total mass concentrations, i.e. the ice water content (IWC) resulting from the mass estimates for the single particles. With the exception of the warmest cloud layer, they are all around 1×10^{-3}–5×10^{-3} g m^{-3}. These values are comparable with the most frequent IWC values of 1–10 ppmv encountered by Luebke *et al.* (2016) in midlatitude in situ origin cirrus; after converting our values to mixing ratios all but the smallest and largest range between about 4 and 17 ppmv. Luebke *et al.* (2013) reported in their climatology of cirrus IWC median values of between about 1 and 10 ppmv for Arctic cirrus in the range of temperatures encountered in our experiments. In their large data set, they saw a decreasing median of IWC values as temperature decreases, whereas in our data there is no clear temperature trend and most PSDs have IWC values similar to the one for the ensemble with the smallest particle and highest number concentration. From the temperature trend of particle sizes, which decrease with decreasing temperature, we expect, if any, only a weak temperature trend (see also the weaker trend in extinction compared to number concentration).

The effective diameter of particle ensembles can be calculated from mass and area concentrations (or IWC and extinction coefficients). We have used the definition by Foot (1988):

$$D_{\text{eff}} = 3/(2\rho_{\text{ice}}) \cdot m/A, \tag{9}$$

where here m and A refer to the total mass and area concentrations, respectively, of a particle ensemble, and not to the single particle properties as elsewhere in this paper.

Figure 15 shows the effective diameters from 10 s averages as a function of altitude, with different colours for the clouds on different days. With

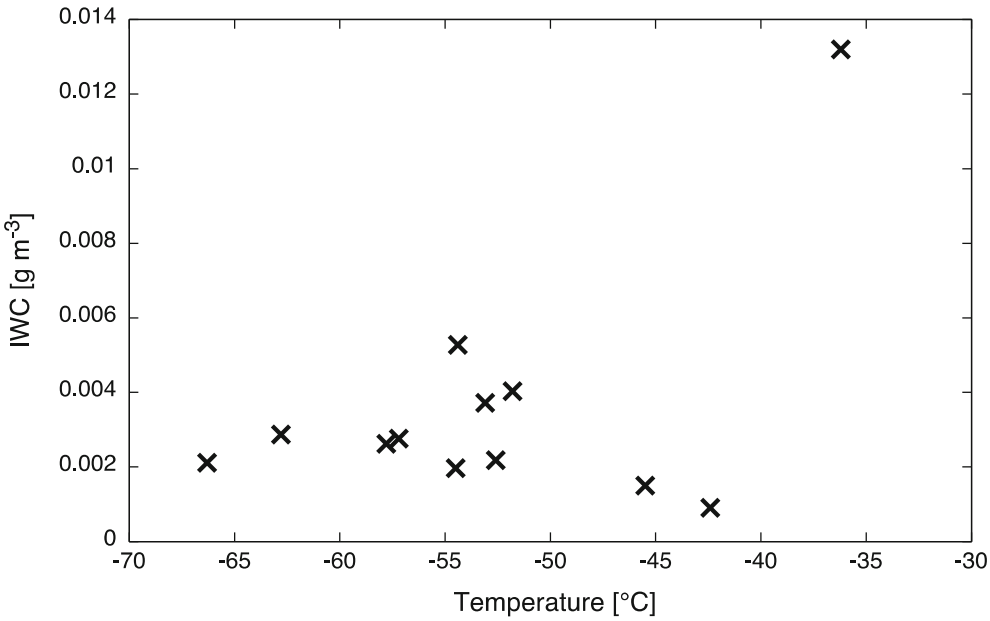

Figure 14
Total mass concentrations, IWC, resulting from the mass estimates for the single particles using Eqs. (8a, 8b)

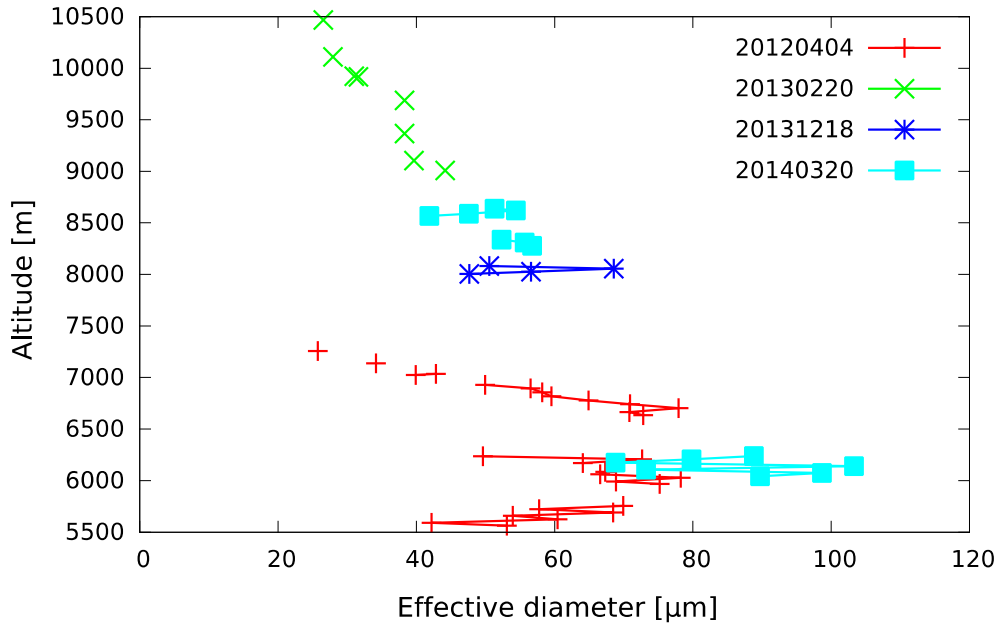

Figure 15
Effective diameters for 10 s average data. *Different colours* show measurements for different days

increasing altitude temperature decreased, and with that the extinction coefficient increased (see Fig. 10), whereas IWC did not vary significantly (see Fig. 14). This results in the decreasing effective diameter with increasing altitude that can be seen in general in Fig. 15.

The effective diameter's dependence directly on temperature is shown in Fig. 16. In addition, it shows the size ranges encountered in the measurements through vertical bars extending from the smallest (MIN) to the largest (MAX) measured particle size (maximum dimension). The average size is also indicated (centre mark on vertical bars), as well as the mass mode diameter of the log-normal mass distribution for the respective particle ensemble. An exponential fit to these mass modes is also shown in the figure and is given by

$$\text{Mass mode} = 3110\,\mu\text{m} \cdot \mathrm{e}^{0.0691 \cdot T/^{\circ}\text{C}}. \qquad (10)$$

Sizes between at the most 500 µm in the highest temperature ensemble and down to 10 µm at temperatures below −55 °C were observed, with averages below 200 µm and corresponding effective diameters below 100 µm. The modal mass diameters reported by Luebke *et al.* (2016) are similar to our mass modes, mostly less than 200 µm.

4. Conclusions

First results from a series of ongoing in situ measurements of high-latitude ice clouds close to Kiruna (northern Sweden) are presented. Ice particles' properties at this Arctic location have been measured with balloon-borne probes that collect and image ice particles with a high optical resolution and a pixel resolution of 1.65 µm. The resulting images clearly showed the shapes of particles larger than about 20 µm and were used to determine the size (maximum dimension), area, and area ratio of individual particles, as well as particle concentrations, PSDs, volume extinction coefficients, and IWC of ensembles of particles.

For each cloud (apart from the optically thinnest cloud), PSDs corresponding to several cloud layers have been analysed. The sample volume of 130 $\text{cm}^3\ \text{s}^{-1}$ of the balloon-borne probe means that at the highest total number concentrations encountered, around 400 L^{-1}, a sample time of 1 s is sufficient to

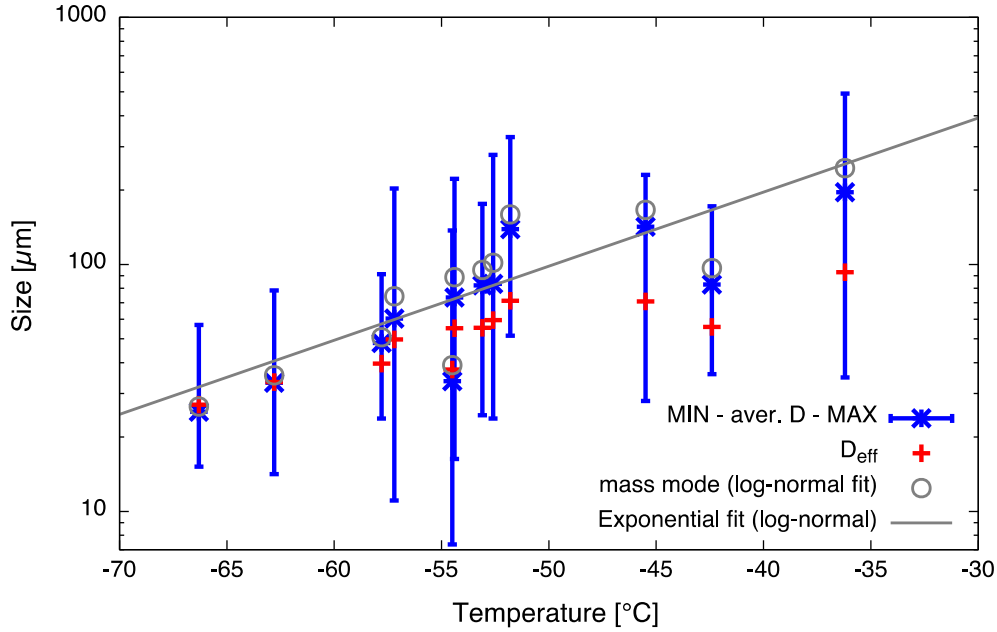

Figure 16
Size ranges of ice particles encountered in different cloud layers are shown as *vertical bars* at the respective average temperatures. The average maximum dimension as well as the effective diameter is *plotted* for each particle ensemble on the corresponding *vertical bar*. The mass mode of the log-normal mass distributions are shown together with a fitted exponential *trend line* (Eq. 10)

determine a PSD. At the lowest concentration of about 4 L^{-1}, corresponding to one particle every 2 s period, about 90 s sample time is required for one PSD. When longer sample times were possible, i.e. for all but the lowest concentration cloud layers, it was observed that fits to both a gamma distribution function, Eq. (1a), and a log-normal distribution, Eq. (1b), achieved very high correlation coefficients, with the log-normal distribution appearing to match the data slightly better. The good agreement also holds when the fitted distributions are converted to area and mass distributions, i.e. the distributions of the important parameters extinction and IWC, respectively. These converted distributions agreed very well with the measured area distribution and the distribution of mass estimated from measured area and maximum dimension. This indicates that for the cold high-latitude ice clouds studied here, the gamma and log-normal distributions are indeed good choices to represent ice particles.

Several properties of these cloud layers have been analysed, in particular with respect to the temperature dependence. The mode size of the PSD has been observed to decrease exponentially with decreasing temperature in the encountered range of −36 to −67 °C. This reflects a general trend of decreasing ice particle sizes with decreasing temperatures. Despite the smaller maximum dimensions at lower temperatures, the volume extinction coefficients increased with decreasing temperatures. This was caused by total particle concentrations that increased by about two orders of magnitude with temperature decreasing over the same range.

Particle areas have been studied and a power law area–dimensional relationship, given by Eq. (5) with $\alpha = 8.23 \times 10^{-13}$ m^2 (D in μm) and $\beta = 1.86$, was found to predict very well the general trend throughout the size range of measured particles of 10 μm to 500 μm. From that, mass estimates were derived based on the measured area and an estimated 'thickness', according to Eqs. (8a, 8b), so that IWC of the cloud layers could be found. While extinction, proportional to area, increased with decreasing temperatures, IWC did not show a clear temperature trend, but fluctuated for all temperatures below −40 °C between about 1×10^{-3}–5×10^{-3} g m^{-3}.

The cold and thin ice clouds measured with the balloon-borne imaging probe described here have

predominantly small ice particles. As could be seen from the presented PSDs, in most cloud layers more than half of the particles had maximum dimensions of below 100 μm. The estimated IWC fraction below 100 μm varied between 1 % and 100 % of total IWC; for half of the analysed cloud layers, it was larger than 50 %. Hence, this confirms how important it is that the balloon-borne imager measured reliably in this size range. Airborne probes would have difficulties measuring such PSDs. Optical array probes, such as the 2D-C, would not provide the same quality data below 100 μm size, and concentrations and sizes would be uncertain. A scattering probe, such as CAS, could have more reliably detected the small particles. However, it would not give images providing particle shapes, and, due to a smaller sample volume would have required an order of magnitude longer sampling times, i.e. around 15 min for the optically thinnest cloud. The CPI, capable of imaging these small particles, has a similar sampling volume as the presented balloon imager; however, larger uncertainties would remain due to shattering and the highly size-dependent sampling volume.

The presented data constitute still a limited data set and the ranges of microphysical properties and average relationships that are found are not necessarily representative. The measured concentrations, however, as well as the PSDs, are reliable and can be used for future studies. In addition, the data analysis presented here shows the usefulness of the collected data, emphasizing the need for continued in situ balloon measurements, which will add to this data set and increase its representativeness for high-latitude, cold ice clouds.

Acknowledgments

We thank the Swedish National Space Board for funding this balloon campaign and the Mesoscale and Microscale Meteorology Laboratory, National Center for Atmospheric Research (NCAR, USA).

References

Baker, B., and R. Lawson (2006a), *In situ observations of the microphysical properties of wave, cirrus, and anvil clouds. Part I: Wave clouds*, J. Atmos. Sci., *63* (12), 3160–3185.

Baker, B., and R. P. Lawson (2006b), *Improvement in determination of ice water content from two-dimensional particle imagery. Part I: Image-to-mass relationships*, J. Appl. Meteorol. Clim., *45*(9), 1282–1290.

Baran, A. J., K. Furtado, L.-C. Labonnote, S. Havemann, J.-C. Thelen, and F. Marenco (2015), *On the relationship between the scattering phase function of cirrus and the atmospheric state*, Atmos. Chem. Phys., *15*(2), 1105–1127, doi:10.5194/acp-15-1105-2015.

Baum, B. A., P. Yang, A. J. Heymsfield, C. G. Schmitt, Y. Xie, A. Bansemer, Y. X. Hu, and Z. Zhang (2011), *Improvements in shortwave bulk scattering and absorption models for the remote sensing of ice clouds*, J. Appl. Meteorol. Clim., *50*, 1037–1056.

Baumgardner, D., and A. Korolev (1997), *Airspeed corrections for optical array probe sample volumes*, J. Atmos. Oceanic Technol., *14*(5), 1224–1229, doi:10.1175/1520-0426(1997)014<1224:ACFOAP>2.0.CO;2.

Baumgardner, D., H. Jonsson, W. Dawson, D. O'Connor, and R. Newton (2001), *The cloud, aerosol and precipitation spectrometer: a new instrument for cloud investigations*, Atmos. Res., *59–60*, 251–264, doi:10.1016/S0169-8095(01)00119-3.

Baumgardner, D., J. E. Dye, B. W. Gandrud, and R. G. Knollenberg (1992), *interpretation of measurements made by the forward scattering spectrometer probe (FSSP-300) during the airborne Arctic stratospheric expedition*, J. Geophys. Res., *97*(D8), 8035– 8046.

Field, P., A. Heymsfield, and A. Bansemer (2006), *Shattering and particle interarrival times measured by optical array probes in ice clouds*, J. Atmos. Oceanic Technol., *23*(10), 1357–1371.

Foot, J. S. (1988), *Some observations of the optical-properties of clouds .2. Cirrus*, Q. J. R. Meteorol. Soc., *114*(479), 145–164, doi:10.1002/qj.49711447908.

Golovin, M. N., and A. A. Putnam, (1962), *Inertial impaction of single elements*, Ind. & Eng. Chem. Fund., *1*, 264–273, doi:10.1021/i160004a007.

Heymsfield, A. J., and L. M. Miloshevich (1995), *Relative humidity and temperature influences on cirrus formation and evolution: Observations from wave clouds and FIRE II*, J. Atmos. Sci., *52*, 4302 – 4326.

Heymsfield, A., A. Bansemer, P. Field, S. Durden, J. Stith, J. Dye, W. Hall, and C. Grainger (2002), *Observations and parameterizations of particle size distributions in deep tropical cirrus and stratiform precipitating clouds: Results from in situ observations in TRMM field campaigns*, J. Atmos. Sci., *59*(24), 3457–3491, doi: 10.1175/1520-0469(2002)059<3457:OAPOPS>2.0.CO;2.

Heymsfield, A. J., A. Bansemer, C. Schmitt, C. Twohy, and M. R. Poellot (2004), *Effective ice particle densities derived from aircraft data*, J. Atmos. Sci., *61*(9), 982–1003.

Heymsfield, A. J., C. Schmitt, and A. Bansemer (2013), *Ice cloud particle size distributions and pressure-dependent terminal velocities from in situ observations at temperatures from 0 to -86 degrees C*, J. Atmos. Sci., *70*(12), 4123–4154, doi:10.1175/JAS-D-12-0124.1.

Heymsfield, A. J., et al. (2008), *Testing IWC retrieval methods using radar and ancillary measurements with in situ data*, J. Appl. Meteorol. Clim., *47*(1), 135–163.

Jackson, R. C., G. M. McFarquhar, J. Stith, M. Beals, R. A. Shaw, J. Jensen, J. Fugal, and A. Korolev (2014), *An assessment of the impact of antishattering tips and artifact removal techniques on cloud ice size distributions measured by the 2D cloud probe*. J. Atmos. Oceanic Technol., *31*, 2567–2590, doi:10.1175/JTECH-D-13-00239.1.

Knollenberg, R. G. (1981), *Techniques for probing cloud microstructure*, in Clouds, Their Formation Optical Properties and Effects, edited by P. Hobbs and A. Deepak, pp. 15–92, Academic Press, New York.

Korolev, A., J. Strapp, and G. Isaac (1998), *Evaluation of the accuracy of PMS Optical Array Probes*, J. Atmos. Oceanic Technol., *15*(3), 708–720.

Korolev, A. V., G. A. Isaac, and J. Hallett (1999), *Ice particle habits in Arctic clouds*, Geophys. Res. Lett., *26*(9), 1299–1302, doi:10.1029/1999GL900232.

Korolev, A. V., S. V. Kuznetsov, Y. E. Makarov, and V. S. Novikov (1991), *Evaluation of measurements of particle size and sample area from optical array probes*, J. Atmos. Oceanic Technol., *8*(4), 514–522, doi:10.1175/1520-0426(1991)008<0514:EOMOPS>2.0.CO;2.

Korolev, A. V., E. F. Emery, J. W. Strapp, S. G. Cober, G. A. Isaac, M. Wasey, and D. Marcotte (2011), *Small ice particles in tropospheric clouds: fact or artifact? airborne icing instrumentation evaluation experiment*, Bull. Amer. Met. Soc., *92*, 967–973, doi:10.1175/2010BAMS3141.1.

Krämer, M. et al. (2016), *A microphysics guide to cirrus clouds – Part 1: Cirrus types*, Atmos. Chem. Phys., *16*, 3463–3483, doi:10.5194/acp-16-3463-2016.

Kuhn, T, and I. Grishin, and J. J. Sloan (2012), *Improved Imaging and Image Analysis System for Application to Measurement of Small Ice Crystals*, J. Atmos. Oceanic Technol., *29*, 1811–1824, doi:10.1175/JTECH-D-11-00199.1.

Lawson, R. P. (2011), *Effects of ice particles shattering on the 2D-S probe*, Atmos. Meas. Tech., *4*(7), 1361–1381, doi:10.5194/amt-4-1361-2011.

Lawson, R. P., B. A. Baker, C. G. Schmitt, and T. L. Jensen (2001), *An overview of microphysical properties of Arctic clouds observed in May and July 1998 during FIRE ACE*, J. Geophys. Res., *106*(D14), 14,989–15,014.

Lawson, R. P., K. Stamnes, J. Stamnes, P. Zmarzly, J. Koskuliks, C. Roden, Q. Mo, M. Carrithers, and G. L. Bland (2011), *Deployment of a tethered-balloon system for microphysics and radiative measurements in mixed-phase clouds at Ny-Ålesund and South Pole*, J. Atmos. Oceanic Technol., *28*(5), 656–670, doi:10.1175/2010JTECHA1439.1.

Luebke, A. E., L. M. Avallone, J. Meyer, C. Rolf, and M. Krämer (2013), *Ice water content of Arctic, midlatitude, and tropical cirrus - Part 2: Extension of the database and new statistical analysis*, Atmos. Chem. Phys., *13*, 6447-6459.

Luebke, A. E., A. Afchine, A. Costa, J.-U. Grooß, J. Meyer, C. Rolf, N. Spelten, L. M. Avallone, D. Baumgardner, and M. Krämer (2016), *The origin of midlatitude ice clouds and the resulting influence on their microphysical properties*, Atmos. Chem. Phys., *16*, 5793–5809, doi:10.5194/acp-16-5793-2016.

Magono, C., and S. Tazawa (1966), *Design of "snow crystal sondes"*, J. Atmos. Sci., *23*, 618–625, doi:10.1175/1520-0469(1966)023<0618:DOCS>2.0.CO;2.

MacCready, P. B., Jr., and C. J. Todd (1964), *Continuous particle sampler*, J. Appl. Meteor., *3*, 450–460.

McFarquhar, G. M., and A. J. Heymsfield (1996), *Microphysical characteristics of three anvils sampled during the Central Equatorial Pacific Experiment*, J. Atmos. Sci., *53*(17), 2401–2423.

Meyers, M. B., and J. Hallett (2001), *Micrometer-sized hygroscopic particles in the atmosphere: Aircraft measurement in the Arctic*, J. Geophys.Res., *106*(D24), 34067–34080.

Miloshevich, L. M., and A. J. Heymsfield (1997), *A balloon-borne continuous cloud particle replicator for measuring vertical profiles of cloud microphysical properties: Instrument design, performance, and collection efficiency analysis*, J. Atmos. Oceanic Technol., *14*(4), 753–768.

Mitchell, D. L., R. P. Lawson, and B. Baker (2011), *Understanding effective diameter and its application to terrestrial radiation in ice clouds*, Atmos. Chem. Phys., *11*, doi:10.5194/acp-11-3417-2011.

Ranz, W. E., and J. B. Wong (1952), *Impaction of dust and smoke particles on surface and body collectors*, Ind. Eng. Chem., *44*(6), 1371–1381, doi:10.1021/ie50510a050.

Schiller, C., M. Krämer, A. Afchine, N. Spelten, and N. Sitnikov (2008), *Ice water content of Arctic, midlatitude, and tropical cirrus*, J. Geophys. Res., *113*, D24208, doi:10.1029/2008JD010342.

Schmitt, C. G., and A. J. Heymsfield (2009), *The size distribution and mass-weighted terminal velocity of low-latitude tropopause cirrus crystal populations*, J. Atmos. Sci., *66*(7), 2013–2028, doi:10.1175/2009JAS3004.1.

Schmitt, C. G., and A. J. Heymsfield (2010), *Dimensional characteristics of ice crystal aggregates from fractal geometry*. J. Atmos. Sci., *67*, 1605–1616.

Sikand, M., J. Koskulics, K. Stamnes, B. Hamre, J. J. Stamnes, R. P. Lawson (2013), *Estimation of mixed-phase cloud optical depth and position using in situ radiation and cloud microphysical measurements obtained from a tethered-balloon platform*, J. Atmos. Sci., *70*(1), 317–329, doi:10.1175/JAS-D-12-063.1.

Spyers-duran, P., and R. Braham (1967), *An airborne continuous cloud particle replicator*, J. Appl. Meteor., *6*, 1108–1113.

Stoelinga, M. T., J. D. Locatelli, and C. P. Woods (2007), *The occurrence of "Irregular" ice particles in stratiform clouds*, J. Atmos. Sci., *64*(7), 2740–2750.

Strapp, J. W., F. Albers, A. Reuter, A. V. Korolev, U. Maixner, E. Rashke, and Z. Vukovic (2001), *Laboratory measurements of the response of a PMS OAP-2DC*, J. Atmos. Oceanic Technol., *18*(7), 1150–1170.

(Received October 5, 2015, revised May 25, 2016, accepted May 26, 2016, Published online June 17, 2016)